

Article

Monitoring Axial Force Development in a Super-Long Pile during Construction Using BOFDA and Data Interpretation Approaches: A Case Study

Dongning Li ¹, Deshan Ma ^{2,3}, Dong Su ^{4,5,*} , Shaohua Rao ¹, Wenbin Wang ^{2,3} and Chengyu Hong ^{4,5} ¹ Shenzhen Talent Housing Group Co., Ltd., Shenzhen 518040, China² China Construction Third Engineering Bureau First Construction Engineering Co., Ltd., Shenzhen 518049, China³ China Construction Third Engineering Bureau (Shenzhen) Co., Ltd., Shenzhen 518049, China⁴ College of Civil and Transportation Engineering, Shenzhen University, Shenzhen 518060, China⁵ Key Laboratory for Resilient Infrastructures of Coastal Cities (MOE), Shenzhen University, Shenzhen 518060, China

* Correspondence: sudong@szu.edu.cn



Citation: Li, D.; Ma, D.; Su, D.; Rao, S.; Wang, W.; Hong, C. Monitoring Axial Force Development in a Super-Long Pile during Construction Using BOFDA and Data Interpretation Approaches: A Case Study. *Buildings* **2022**, *12*, 1462. <https://doi.org/10.3390/buildings12091462>

Academic Editors: Bingxiang Yuan, Yong Liu, Xudong Zhang and Yonghong Wang

Received: 8 August 2022

Accepted: 10 September 2022

Published: 15 September 2022

Publisher's Note: MDPI stays neutral with regard to jurisdictional claims in published maps and institutional affiliations.



Copyright: © 2022 by the authors. Licensee MDPI, Basel, Switzerland. This article is an open access article distributed under the terms and conditions of the Creative Commons Attribution (CC BY) license (<https://creativecommons.org/licenses/by/4.0/>).

Abstract: Long-term monitoring data for super-long piles are scarce and valuable. This paper reports axial strain measurements of a cast-in-place large-diameter pile embedded 76.7 m into a “weathered trench” of granite in Nanshan District, Shenzhen, China, using BOFDA monitoring technology. An approach based on the load-transfer method to interpret data is proposed, in which the axial load at the pile head and the shear behavior at the pile–soil interface can be analyzed. Results show that these data can well reflect the increase in axial strain as the number of floors built increases, although there is deviation related to fiber cable bending due to the installation and compaction of concrete, and the complex loading condition at the pile head. Sensitivity analysis of parameters disclosed that the friction angle between the soil and the pile was approximately 10° for the cast-in-place pile monitored in this study, which is approximately one third of the interface friction angle, considering the slurry cake effect. The average axial force exerted on the pile head induced by building one floor ranged from 116.00 kN to 297.43 kN; this increased with the number of floors built and the total loads of the superstructure. This implies that the raft carried a large portion of the structural load during the early construction stage; piles gradually carried a major portion of the increased load due to continuous construction. The overall mobilized percentage of skin friction was approximately 40.8% when 40 floors were built, and the pile had the potential to carry more axial load.

Keywords: super-long pile; Brillouin Optical Frequency Domain Analysis (BOFDA); load-transfer method; axial strain; skin friction

1. Introduction

Pile foundations are widely adopted to support heavy structures, such as high-rise buildings [1] and river bridges [2], due to their significant vertical and horizontal bearing capacities and the advantages that they provide in controlling long-term displacement. In many situations, for the sake of both economy and safety, piles are combined with rafts to form piled raft foundations for super high-rise buildings, for which the soil–pile–structure interaction is a complex problem. Approaches used to investigate piles or piled raft foundations’ behaviors primarily include 1 g or centrifuge experiments, numerical studies, and field measurements. Experimentally, small-scale tests facilitate extensive investigation of the effects of pile number, pile size, embedment length, pile spacing, and soil type on the group interaction or the load sharing of piled raft foundations (e.g., [3–14]). However, due to model size limitations, the scale effect and boundary effect are sometimes unavoidable, which hinders the extension of laboratory observations directly to the interpretation or design of real foundations. Full-scale field tests and field monitoring, despite their relatively high cost, can produce limited but valuable results (e.g., [15–21]). Full-scale tests

include short-term measurement as well as long-term observation during and following the construction period. To investigate the bearing behavior of super-long piles located in deep soft clay over stiff layers, Zou and Zhao [22] conducted a field load test of a pile with a diameter of 1.0 m and a length of 60 m. Wang et al. [23] performed a static load test on three super-long bored piles of diameter 1.5 m and length 80 m in deep fine silty sand layers. Li et al. [24] investigated two cast-in-situ bored piles of length 56.5 m and 56.6 m subjected to compressive load. Feng et al. [25] carried out field investigations of two super-long steel pipe piles of length 85.7 m and 78.7 m in offshore areas. There are two main numerical approaches for analyzing pile behaviors. First, in the finite element and finite difference method, soils around the piles are treated as continuum media, and soil–pile–structure interactions are modeled directly (e.g., [26–29]). In the second approach, the pile is modeled as an elastic member, whereas the soil is idealized as a discrete set of independent springs that describes the soil–pile interaction. This includes the “p-y” method for laterally loaded piles (e.g., [30–32]) and the “t-z” method for vertically loaded piles (e.g., [33,34]).

Long-term monitoring of pile behaviors, especially cast-in-place piles, involves harsh conditions; sensors must be durable, stable, and have a high survival rate. In recent years, optical fiber sensing technology has become popular for engineering monitoring [35,36] due to its good performance under various conditions. Fiber Bragg gratings (FBGs), an optical fiber technology, have been used to measure the distribution of strain, temperature, and displacement in civil engineering for both slopes [37,38] and piles [39]. Distributed optical fiber monitoring technologies such as Brillouin optical time domain analysis (BOTDA) [40], Brillouin optical time domain reflectors (BOTDR) [41], Brillouin optical frequency domain reflectors (BOFDA) [42], optical frequency domain reflectometers (OFDR) [43], and distributed optical fiber sensors (DOFS) [44] have also been widely adopted in engineering monitoring. For example, Gao et al. [45] used OFDR technology to measure the deformation characteristics of a PCC pile in small model tests. Liu et al. [46] adopted OFDR optical fiber sensing technology to measure the horizontal strain of a pile in a cross-rock pillar excavation model test. Based on DOFS–BOTDA monitoring technology, Wei et al. [47] measured the internal force of an anti-slide pile in Badong No. 3 High School; monitoring data verified the long-term effectiveness of anti-slide pile management and the superiority of the monitoring technology.

This study focuses on the long-term behavior of super-long cast-in-place piles. A concrete pile 76.7 m in length and 1.6 m in diameter, embedded mainly in strongly weathered granite, was monitored using BOFDA technology. The development of axial strain in the pile during superstructure construction was measured. An approach based on the load-transfer method is proposed to interpret data and identify and describe the development of the axial load at the pile head and skin friction along the pile shaft. These results will provide a further understanding of the bearing mechanism of super-long piles in this project, and provide a good reference for similar projects.

2. Monitoring of Pile Axial Force during Construction

2.1. Engineering Project

As shown in Figure 1, the construction site is located in the high-tech industrial park on Baishi Road, Nanshan District, Shenzhen, China, to the north of Baishi Road, to the east of Keji South Road, to the south of Gaoxin South 4th Road, and to the west of Keji South 8th Road. To allow for new building construction, one commercial building and eight multi-story residential buildings were demolished, including three 62-story residential buildings, three 44/45-story residential buildings, and other ancillary podium buildings. Figure 1 provides an aerial photo showing these buildings' foundation pits.

According to the drilling exposure, strata at the site, from top to bottom are: quaternary Holocene artificial fill layer (Q_4^{ml}), quaternary Holocene marine continental interactive sediment layer (Q_4^{mc}), quaternary Holocene alluvial proluvial layer (Q_4^{mc}), quaternary eluvial soil layer (Q^{el}), and underlying bedrock consisting of Yanshanian phase IV (early Cretaceous) granite ($\eta\beta^5K_1$). Pile foundations were adopted to support high-rise buildings

in this project. Piles penetrated through strata primarily consisting of gravelly clayey soil, completely weathered granite, earthy strongly weathered granite, fragmentary strongly weathered granite, moderately weathered granite, and slightly weathered granite. Samples obtained from boreholes are presented in Figure 2. The soils' mechanical properties, as provided by the survey unit, are presented in Table 1. The main characteristics of these strata are as follows:

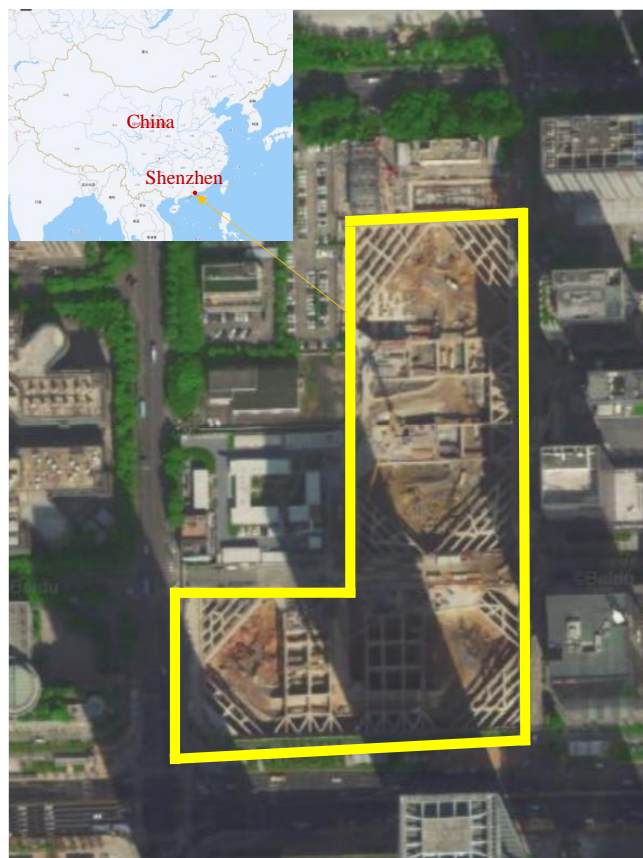


Figure 1. The site and foundation pits of the engineering project.

(1) Gravelly clayey soil is maroon, gray–white, isabelline yellow, and other colors. It is in a plastic to hard-plastic state and contains 20–25% quartz gravel, which is the weathered residual soil of biotite granite. Some boreholes reveal that this layer is significantly kaolinized, and it collapses easily in water. This layer is widely distributed throughout the site, is 1.50–28.80 m thick, with an average thickness of 13.95 m, a top burial depth of 5.20–18.90 m, and a bottom depth of 13.50–42.40 m. The core recovery rate of this layer is 80–95%.

(2) Completely weathered granite is maroon, brown–yellow, or brown–gray. The rock is intensively weathered; its organizational structure is damaged, but it is still recognizable. The rock core is hard soil, the alloy can be drilled, and it collapses easily in water. The rock is extremely broken and classified as extremely soft rock. The rock mass is basic quality grade V. This layer is widely distributed throughout the site, is 1.50–19.20 m thick, has a top buried depth of 11.80–42.40 m, and a bottom depth of 22.00–49.00 m. The core recovery rate of this layer is 80–90%.

(3) Earthy strongly weathered granite is brownish yellow and brownish gray. Most of the original rock structure is damaged and most of the minerals, except quartz, have been weathered into sandy soil. The rock core is relatively hard soil that can be crushed by hand; it disintegrates easily in water, and dry drilling is possible. There are strongly weathered rock fragments or moderately weathered rock blocks at the bottom in some locations. The rock is extremely broken and classified as extremely soft rock. The rock mass is basic quality grade V. This layer is widely distributed throughout the site, is 2.50–37.80 m

thick, has a top buried depth of 16.40~49.00 m, and a bottom depth of 43.50~62.50 m. The core recovery rate of this layer is 75–90%.

(4) Fragmentary strongly weathered granite is brown–yellow, flesh red, and other colors. Most of the original rock structure is damaged; it has a granite structure, very developed joints, and some portions rendered by iron oxides. The rock core is broken, soft rock, mostly fragmentary in shape, and fragile when hammered. The rock is extremely broken and classified as extremely soft rock. The rock mass is basic quality grade V. This layer is widely distributed throughout the site, is 0.70~11.70 m thick, has a top buried depth of 44.10~59.60 m, and a bottom depth of 46.60~63.30 m. The core recovery rate of this layer is 70–80%.

(5) Moderately weathered granite is flesh red and has a massive granite structure with structural fissures affected by nearby structural fractures. Rock cores are mostly fragmentary with short columnar structures and some localized long columnar structures. The structure is partially damaged, difficult to break, and has a crisp hammering sound. The rock mass is relatively broken and basic quality grade IV (RQD = 10~60). This layer is widely distributed throughout the site, has a top elevation of –59.34~–39.09 m, and a top buried depth of 43.50~63.30 m. The core recovery rate of this layer is 70–80%.

(6) Slightly weathered granite is flesh red and has a massive granite structure with slightly developed fissures. The rock core has a long columnar structure with few fragments and a brittle rock block hammering sound. The rock is relatively broken ~ relatively complete and basic quality grade IV ~ II (RQD = 20~80). It has a top elevation of –62.20~–44.67 m and a top buried depth of 49.40~66.80 m. The core recovery rate of this layer is 75–90%.

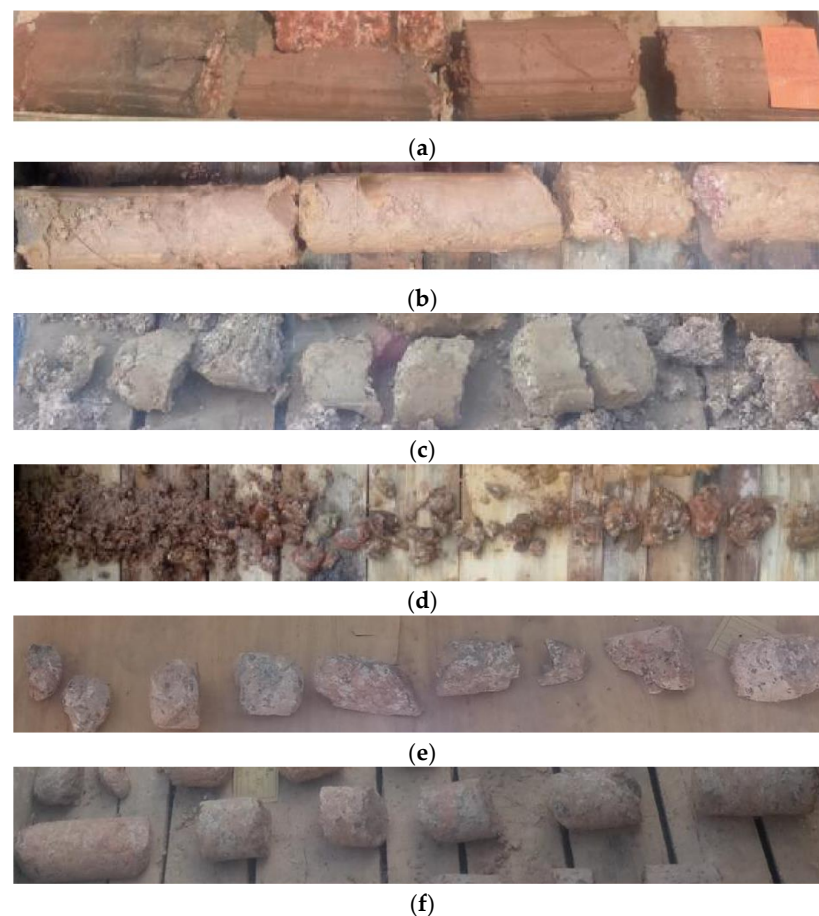


Figure 2. Soil/rock samples from bore holes: (a) gravelly clayey soil; (b) completely weathered granite; (c) earthy strongly weathered granite; (d) fragmentary strongly weathered granite; (e) moderately weathered granite; (f) slightly weathered granite.

Table 1. The mechanical properties of soils.

Soil	Unit Weight, γ (kN/m ³)	Compression Modulus, E_s (MPa)	Friction Angle, φ (°)	Cohesion, c (kPa)
Gravelly clayey soil	19.0	8	25	22
Completely weathered granite	20.0	12	28	25
Earthy strongly weathered granite	21.0	16	30	28
Fragmentary strongly weathered granite	22.0	/	33	28
Moderately weathered granite	23.0	/	/	/

The project’s foundation adopted large-diameter (1.2~1.8 m) bored cast-in-place piles in combination with a raft. After the pile foundation construction unit entered the site, it was found that, according to advance drilling data, the largest buried depth of the moderately weathered rock surface in the middle area of a tower in the north area was approximately 100 m; the height difference in the bearing layer between the pile foundations in the tower area was approximately 40 m. The survey unit preliminarily judged that there was a “weathered trench” in the tower site of a dormitory in the north area, because the site was located in the fracture-affected area. Affected by the fracture, the weathered layer was uneven; the thickness of the local weathered layer changed greatly, and the bedrock was broken.

Pile A50, as illustrated in Figure 3, was located in the “weathered trench”. The pile was 1.6 m in diameter and 76.7 m in effective length. As shown in Figure 4, pile skin friction was mainly provided by the strata of completely weathered granite and strongly weathered granite (although the strongly weathered granite contains thin interlayers of slightly weathered granite), whereas the end bearing capacity was provided by slightly weathered granite. The piles were cast in place; pile holes were formed using a rotary drilling method and holes’ walls were protected by slurry. The effect of residual slurry on skin friction between piles and surrounding soils should be carefully considered.

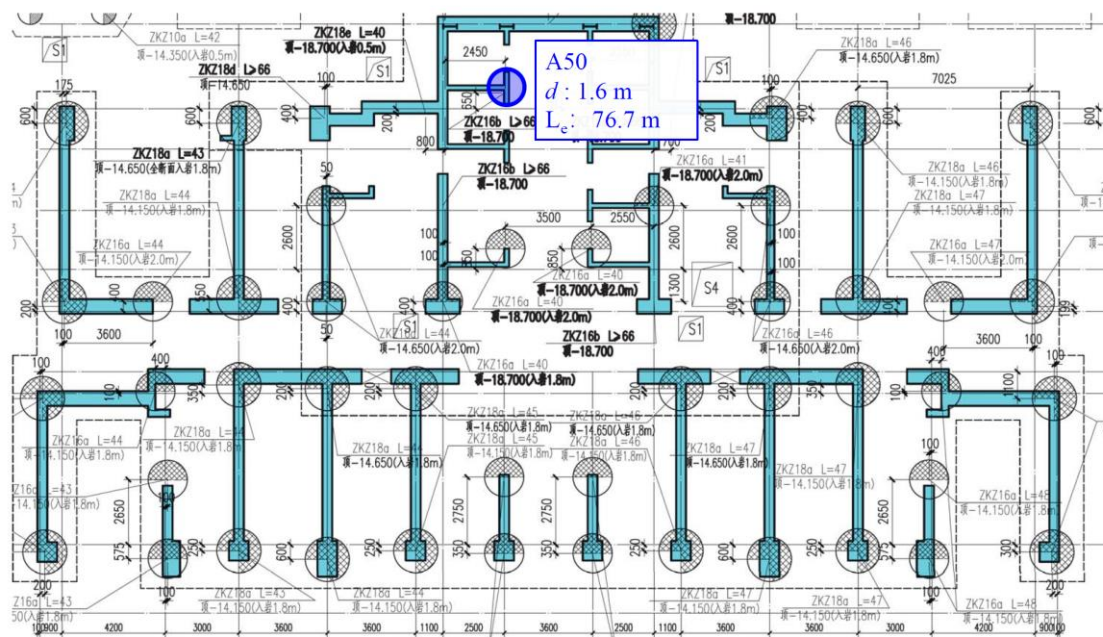


Figure 3. The location of Pile A50.

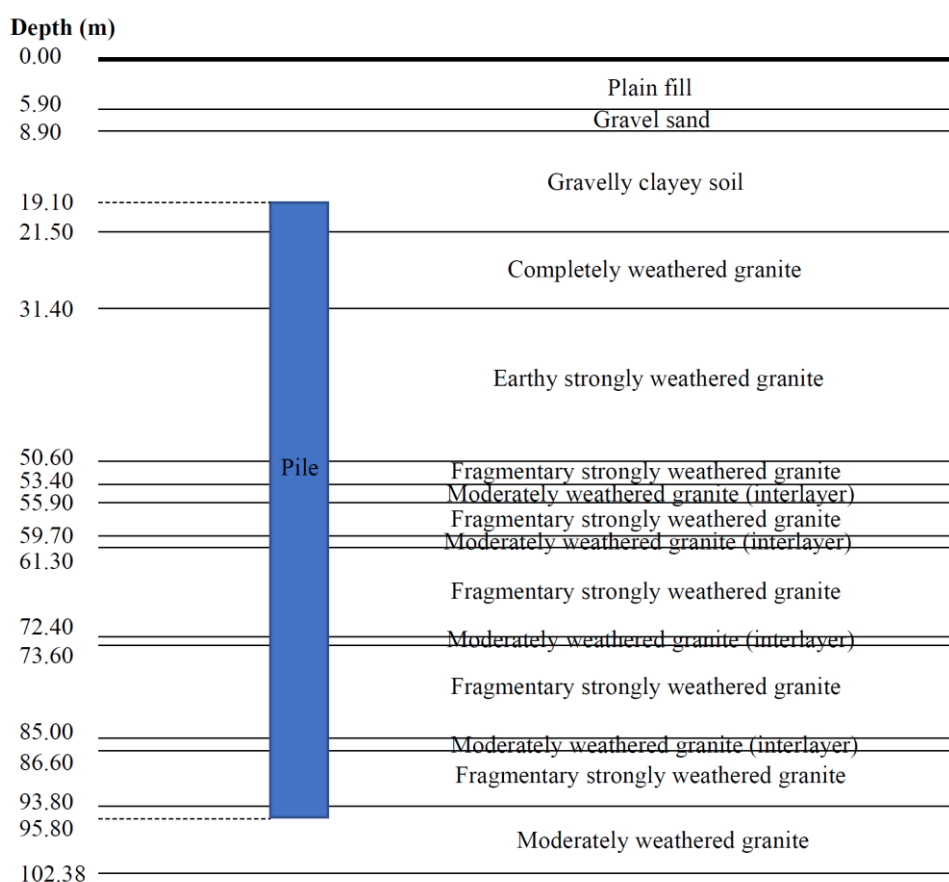


Figure 4. The stratum of Pile A50.

2.2. Sensors and Installation

This project used Brillouin optical frequency domain analyzer (BOFDA) monitoring technology to better understand pile behavior in the “weathered trench”. The BOFDA’s basic sensing principle is shown in Figure 5. Light from a narrow-linewidth pump laser is coupled to one end of a single-mode fiber, and the light from a narrow-linewidth probe laser is coupled at the other end. The pump laser’s frequency is decreased by an amount equal to the fiber’s Brillouin frequency. The characteristic frequency of a standard telecom single-mode fiber is approximately 13 GHz. The probe laser’s light achieves an amplitude with a variable angular modulation frequency. The BOFDA measurement principle is that alternate parts of the modulated probe and modulated pump intensities are recorded at the sensor fiber’s end for each probe light. Herein, a pump wave probe induces Brillouin loss. The photodetector’s output signal is transmitted to the frequency analyzer, which determines the baseband transfer function of the tested fiber optic sensor. Next, the baseband transfer function is input to the signal processor to calculate the inverse fast Fourier transform (IFFT). This IFFT approximates the impulse response of the tested fiber optic sensor and is similar to the temperature and strain profiles along the fiber.

Figure 6 illustrates fiber optic sensor installation along piles. Four distributed strain sensors and two distributed temperature sensors were installed from pile top to pile bottom to measure strain and monitor temperature. Specifically, sensors were symmetrically placed along the longitudinal bars of a steel cage with rolled belts, forming a U-shaped loop (as shown in Figure 6a) and fixed using 1–2 m spacing. Sensors were placed inside a steel cage to avoid direct contact with the surrounding rock, soil mass, and perfusion equipment, as presented in Figure 6b. Two FBG sensors were also placed on the same longitudinal bar to calibrate strain measurements from the distributed fiber sensors.

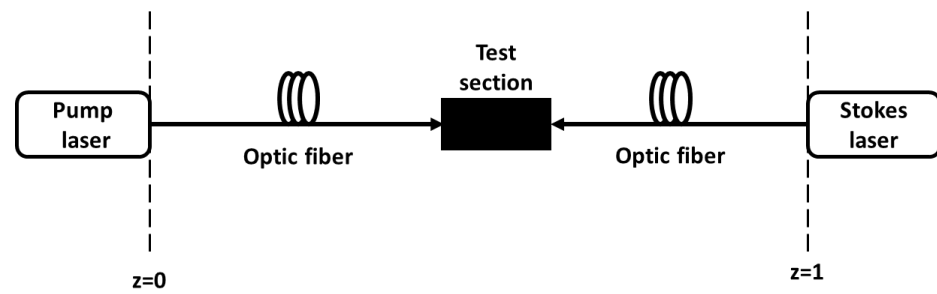
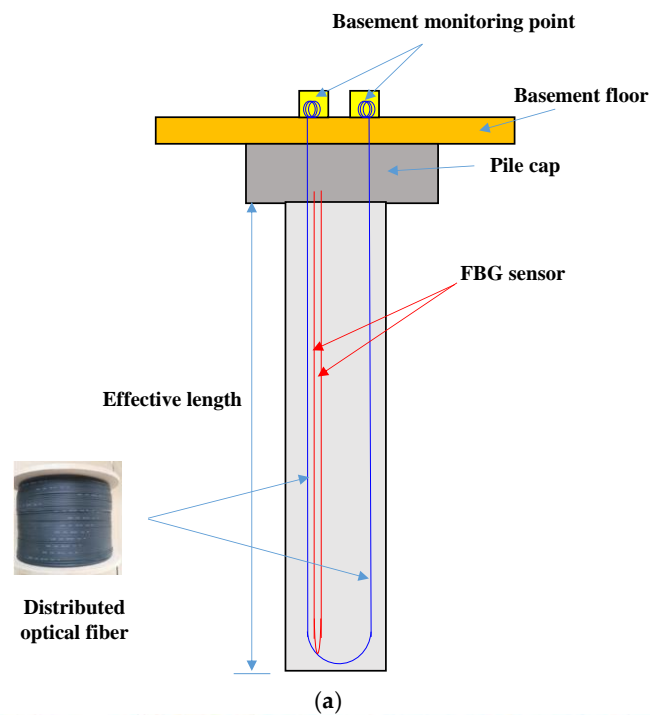


Figure 5. Basic measurement principle of BOFDA.



(a)



(b)

Figure 6. Sensor layout scheme: (a) sensor layout; (b) field installation.

2.3. Measurement Results

Figure 7 shows raw BOFDA measurement data collected during construction; on 14 November 2021, 26 November 2021, 5 December 2021, 14 December 2021, 2 January 2022, 19 February 2022, 9 March 2022, 18 May 2022, and 29 May 2022, the number of floors built was 13, 17, 19, 20, 24, 28, 31, 36, and 40, respectively. Measured axial strain increased with each increase in floor number and the superstructure's weight. Generally, strain decreases with increasing depth; however, significant local variation is likely due to the bending of the fiber cable during concrete installation and compaction. The magnitude of change in the strain between depths of 10 m and 15 m seemed to be unreasonably large, which was probably due to the complex loading condition at the pile head. Therefore, it was not feasible to calculate the axial load at the pile head directly from raw data.

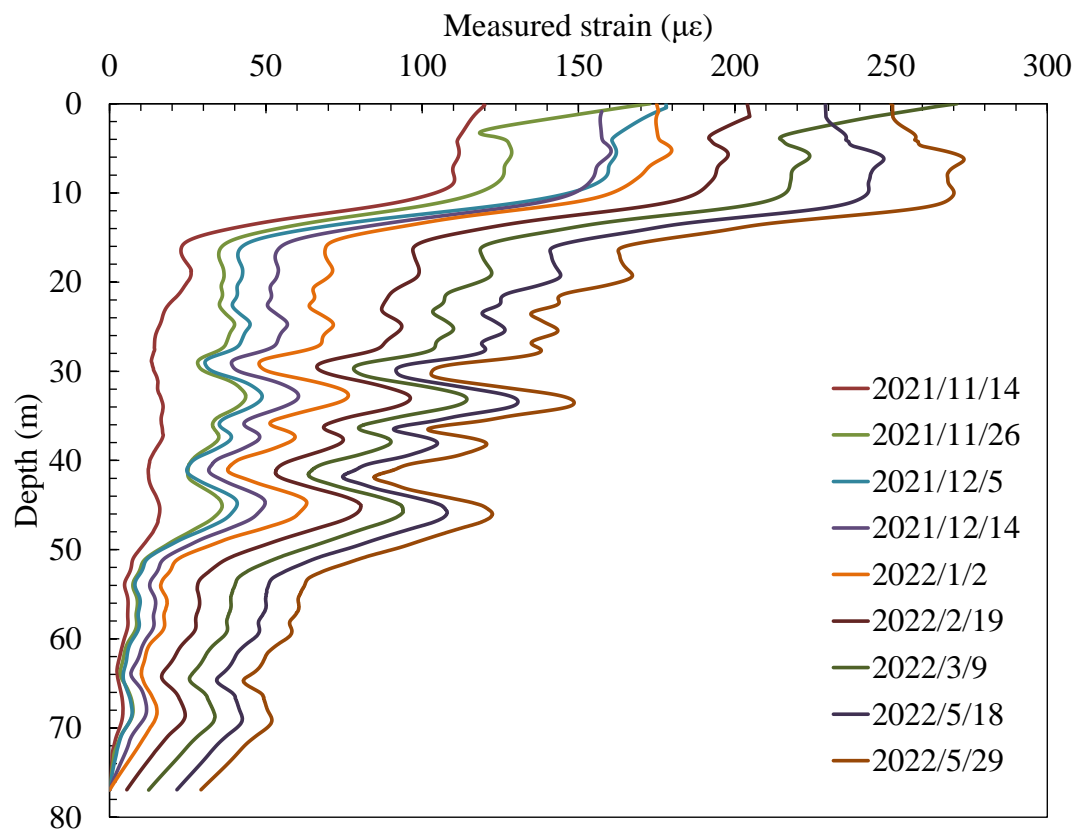


Figure 7. Measured strain during construction of building.

3. The Approach for the Interpretation of Measured Data

3.1. Methodology

This study used the load-transfer method to interpret raw data. As shown in Figure 8, the pile was divided into a certain number of elements along the axial direction. Based on the force equilibrium of each element, the relation matrix between the force at the top of the pile and the axial strain of each element was obtained. Assuming that the soil–pile interface behavior followed the bilinear model (as shown in Figure 9), the matrix could be solved for any given axial load at the top of the pile and corresponding axial strains for each element can be determined. Next, calculated axial strains under different axial loads were compared with measured data, and the best-fit case was considered as the true response of the vertically loaded pile. The process used is as follows.

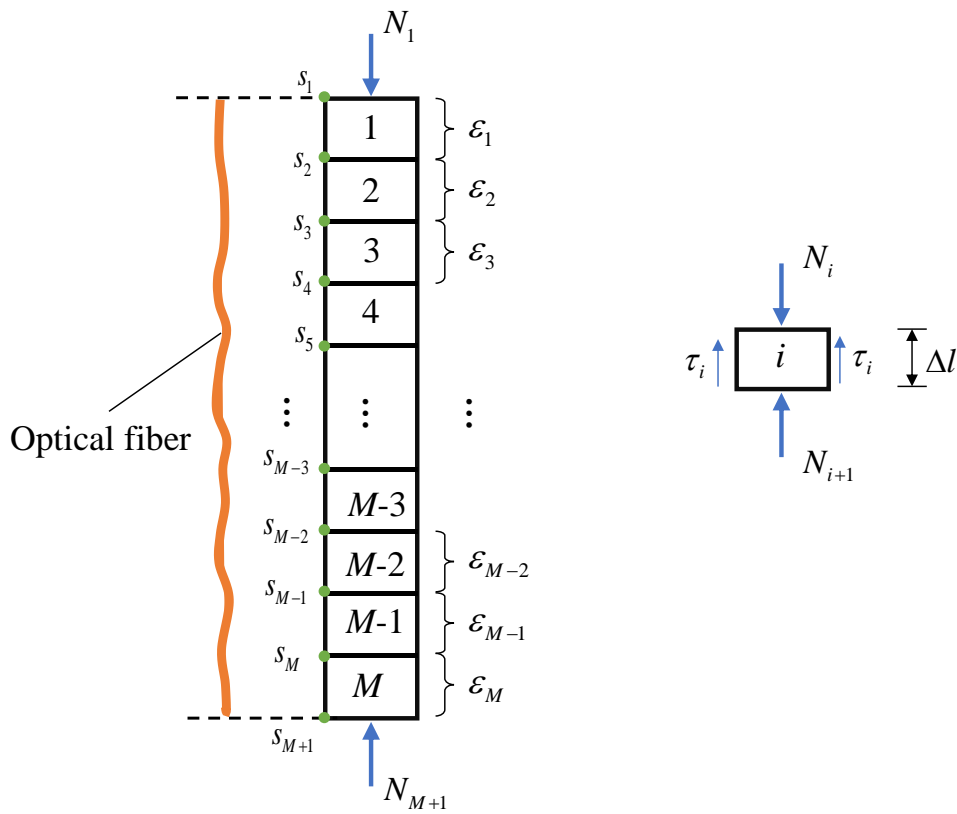


Figure 8. Illustration of methodology for data interpretation.

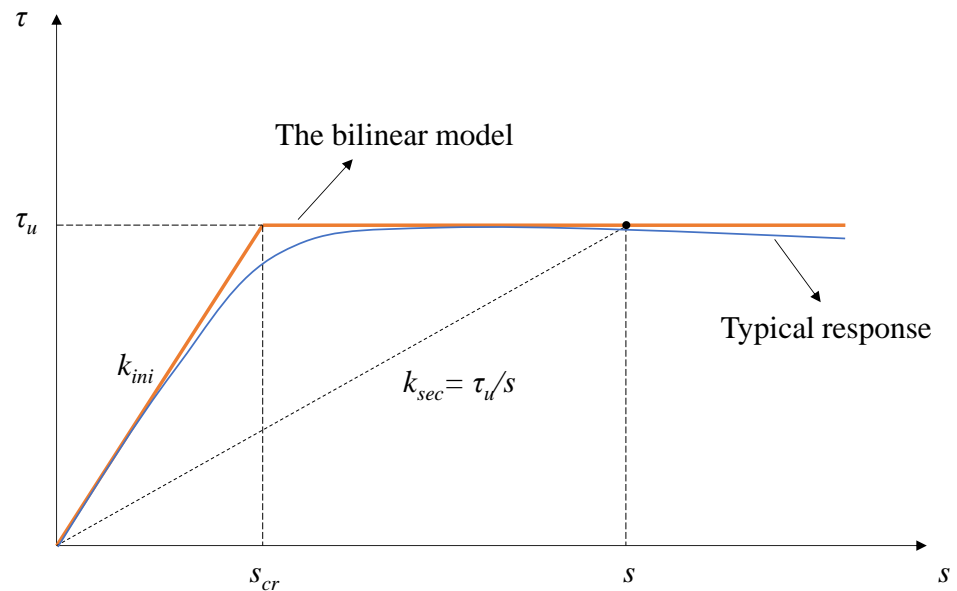


Figure 9. The bilinear model for the interface behavior.

First, the pile is divided into M elements with an equal length of Δl , as shown in Figure 8. It is assumed that the axial strain in the i^{th} element is ε_i when the axial load at the top of the pile is N_1 . At the same time, the axial forces are N_i and N_{i+1} at the top and bottom of the element, respectively, and the corresponding vertical displacements are s_i and s_{i+1} , respectively. Based on the linear and elastic relationship of the pile,

$$N_{i+\frac{1}{2}} = \frac{1}{2}(N_i + N_{i+1}) = A_p \sigma_i = E A_p \varepsilon_i \quad (1)$$

where $N_{i+\frac{1}{2}}$ is the average axial force of the i^{th} element, A_p is the cross-sectional area of the pile, and E is the Young's modulus of the pile.

According to force equilibrium, the force at the bottom of the i^{th} element can be determined by

$$N_{i+1} = N_i - \Delta N_i = N_1 - (\Delta N_1 + \Delta N_2 + \Delta N_3 + \dots + \Delta N_i) \quad (2)$$

where ΔN_i is the difference between N_{i+1} and N_i . As shown in Figure 8, the force difference is balanced by the frictional force mobilized along the interface between the pile and the surrounding soil, i.e.,

$$\Delta N_i = \tau_i u \Delta l \quad (3)$$

where τ_i is the mobilized shear stress at the interface of the i^{th} element, and u is the pile's perimeter.

The magnitude of mobilized shear stress around the pile depends on the relative vertical displacement between the pile and the surrounding soil (denoted by s) when the pile is loaded at the pile head. This relationship can be readily determined using the direct shear of the interface between the soil and a concrete block (mimicking the pile). Usually, the behavior can be approximately described using the bilinear model, as shown in Figure 9. The bilinear model is characterized by three parameters: initial stiffness, k_{ini} ; ultimate shear strength, τ_u ; and critical displacement, s_{cr} . The mobilized shear stress, τ_i , can be determined as

$$\tau_i = k_i s_{i+\frac{1}{2}} = \frac{1}{2} k_i (s_i + s_{i+1}) \quad (4)$$

where $s_{i+\frac{1}{2}}$ is the average relative displacement of the i^{th} element of the pile against the surrounding soil, and k_i is the equivalent stiffness. $s_{i+\frac{1}{2}}$ is calculated using

$$s_{i+\frac{1}{2}} = \frac{1}{2} (s_i + s_{i+1}) \quad (5)$$

Next, s_i and s_{i+1} can be expressed by the vertical displacement at the top of the pile, s_1 , and the strains, ε_i , as follows:

$$s_i = s_1 - (\varepsilon_1 + \varepsilon_2 + \dots + \varepsilon_{i-1}) \Delta l \quad (6)$$

$$s_{i+1} = s_1 - (\varepsilon_1 + \varepsilon_2 + \dots + \varepsilon_i) \Delta l \quad (7)$$

On the other hand, the equivalent stiffness, k_i , is

$$k_i = k_{ini} \text{ when } s_{i+\frac{1}{2}} < s_{cr} \quad \text{or} \quad (8a)$$

$$k_i = k_{sec} = \frac{\tau_u}{s} \text{ when } s_{i+\frac{1}{2}} \geq s_{cr} \quad (8b)$$

Combining Equations (3)–(7), one has

$$\begin{aligned} \Delta N_i &= \frac{1}{2} k_i (s_i + s_{i+1}) u \Delta l \\ &= k_i \left(\frac{s_1}{\Delta l} - \varepsilon_1 - \varepsilon_2 - \dots - \varepsilon_{i-1} - \frac{1}{2} \varepsilon_i \right) u (\Delta l)^2 \\ &= k_i B \left(\frac{s_1}{\Delta l} - \varepsilon_1 - \varepsilon_2 - \dots - \varepsilon_{i-1} - \frac{1}{2} \varepsilon_i \right) \end{aligned} \quad (9)$$

where $B = u(\Delta l)^2$. Next, based on Equations (1), (2), and (9), one has

$$\begin{aligned} &\left(\frac{1}{2} k_1 + k_2 + k_3 + \dots + k_{i-1} + \frac{1}{2} k_i \right) \varepsilon_1 + \left(\frac{1}{2} k_2 + k_3 + \dots + k_{i-1} + \frac{1}{2} k_i \right) \varepsilon_2 \\ &+ \left(\frac{1}{2} k_3 + k_4 + \dots + k_{i-1} + \frac{1}{2} k_i \right) \varepsilon_3 + \dots + \left(\frac{1}{2} k_{i-1} + \frac{1}{2} k_i \right) \varepsilon_{i-1} \\ &+ \left(\frac{1}{4} k_i - \frac{EA_p}{B} \right) \varepsilon_i = -\frac{N_1}{B} + \frac{s_1}{\Delta l} \left(k_1 + k_2 + \dots + k_{i-1} + \frac{1}{2} k_i \right) \end{aligned} \quad (10)$$

On the right side of Equation (10), s_1 remains unknown and needs to be resolved or replaced. To this end, the axial force at the bottom of the pile, N_{M+1} , is assumed to be linearly related to the pile displacement at the location, i.e.,

$$N_{M+1} = A_p k_b s_{M+1} \tag{11}$$

where k_b is the stiffness at the bottom of the pile, and s_{M+1} is the pile displacement at the bottom, and can be calculated using

$$s_{M+1} = s_1 - (\varepsilon_1 + \varepsilon_2 + \dots + \varepsilon_M)\Delta l \tag{12}$$

Let $I = M$ in Equation (2), and substituting Equation (7) into Equation (2) yields

$$N_{M+1} = N_1 - B \frac{s_1}{\Delta l} (k_1 + k_2 + \dots + k_M) + B \left[\left(\frac{1}{2}k_1 + k_2 + k_3 + \dots + k_M \right) \varepsilon_1 + \left(\frac{1}{2}k_2 + k_3 + \dots + k_M \right) \varepsilon_2 + \left(\frac{1}{2}k_3 + \dots + k_M \right) \varepsilon_3 + \dots + \frac{1}{2}k_M \varepsilon_M \right] \tag{13}$$

Combining Equations (11) and (12), one has

$$s_1 = \frac{1}{A} \left\{ N_1 + A_b k_b (\varepsilon_1 + \varepsilon_2 + \dots + \varepsilon_M) \Delta l + B \left[\left(\frac{1}{2}k_1 + k_2 + k_3 + \dots + k_M \right) \varepsilon_1 + \left(\frac{1}{2}k_2 + k_3 + \dots + k_M \right) \varepsilon_2 + \left(\frac{1}{2}k_3 + \dots + k_M \right) \varepsilon_3 + \dots + \frac{1}{2}k_M \varepsilon_M \right] \right\} \tag{14}$$

where $A = A_b k_b + \frac{B}{\Delta l} (k_1 + k_2 + \dots + k_M)$.

Finally, substituting Equation (14) into Equation (10) yields

$$\begin{aligned} & \left\{ \left(\frac{1}{2}k_1 + k_2 + \dots + k_{i-1} + \frac{1}{2}k_i \right) - \left[\left(\frac{1}{2}k_1 + k_2 + \dots + k_M \right) B + A_b k_b \Delta l \right] C_i \right\} \varepsilon_1 \\ & + \left\{ \left(\frac{1}{2}k_2 + k_3 + \dots + k_{i-1} + \frac{1}{2}k_i \right) - \left[\left(\frac{1}{2}k_2 + k_3 + \dots + k_M \right) B + A_b k_b \Delta l \right] C_i \right\} \varepsilon_2 + \dots \\ & + \left\{ \left(\frac{1}{2}k_{i-1} + \frac{1}{2}k_i \right) - \left[\left(\frac{1}{2}k_{i-1} + k_i + \dots + k_M \right) B + A_b k_b \Delta l \right] C_i \right\} \varepsilon_{i-1} \\ & + \left\{ \left(\frac{1}{4}k_i - \frac{EA_b}{B} \right) - \left[\left(\frac{1}{2}k_i + k_{i+1} + \dots + k_M \right) B + A_b k_b \Delta l \right] C_i \right\} \varepsilon_i \\ & - \left[\left(\frac{1}{2}k_{i+1} + k_{i+2} + \dots + k_M \right) B + A_b k_b \Delta l \right] C_i \varepsilon_{i+1} - \dots - \left[\frac{1}{2}k_M B + A_b k_b \Delta l \right] C_i \varepsilon_M \\ & = \left(C_i - \frac{1}{B} \right) N_1 \end{aligned} \tag{15}$$

where $C_i = \frac{1}{A \Delta l} (k_1 + k_2 + \dots + k_{i-1} + \frac{1}{2}k_i)$.

For $I = 1$ to M , Equation (15) provides algebraic equation groups that describe the relationship between the force at the top of the pile and the axial strain of each element. Algebraic equation groups are then solved for different axial loads at the pile head (such as $N_1^1, N_1^2, \dots, N_1^p$), and the corresponding strains, ε_i^j ($1 \leq i \leq M, 1 \leq j \leq p$), are also solved. The Euclidean distances between these strains and measured data are calculated for each N_1 as follows:

$$d_j = \sqrt{\sum_{i=1}^M (\varepsilon_i^j - \varepsilon_i^m)^2} \quad (1 \leq j \leq p) \tag{16}$$

The trial load at the pile head (i.e., N_1) that yielded the minimum Euclidean distance was considered the true force exerted on the pile head; the corresponding calculated strains were considered the true responses along the pile, as illustrated in Figure 10.

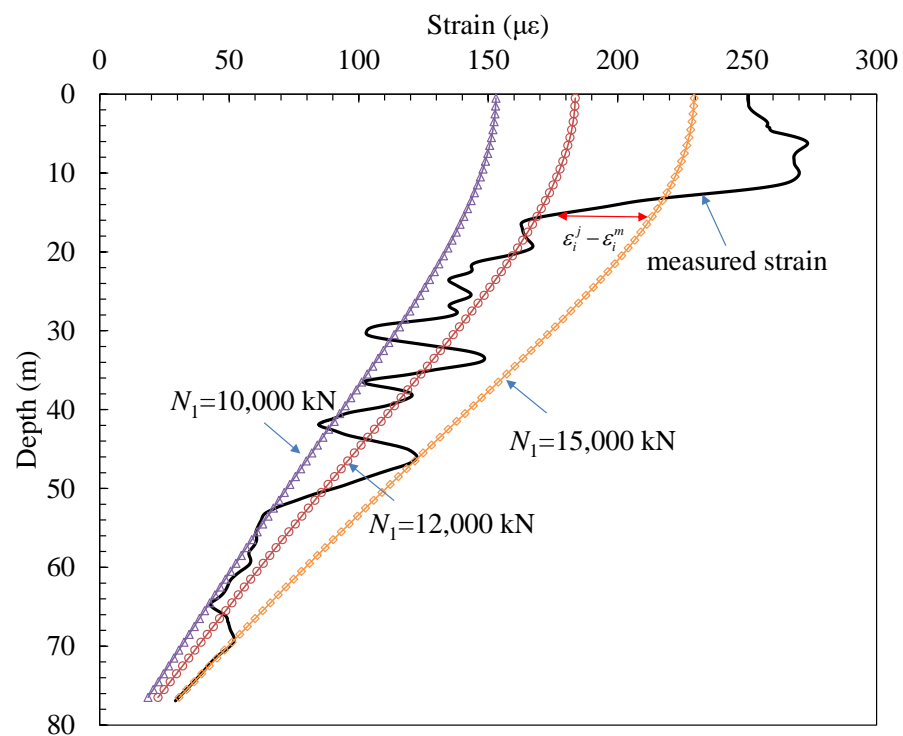


Figure 10. Determination of the load at the pile head by the minimum Euclidean distance.

3.2. Interpretation of Measured Data

To interpret measured strain data using the methodology presented in the previous section, it was important to determine the ultimate skin friction between the soil and the pile, which is usually calculated using

$$\tau_u = \sigma_h \tan \alpha = k_0 \sigma_v \tan \alpha \quad (17)$$

where σ_h is the lateral soil stress acting on the pile skin, σ_v is the vertical stress, k_0 is the coefficient of lateral Earth pressure, and α is the friction angle at the soil–pile interface. Vertical stress is calculated based on the soil's unit weight. The coefficient of lateral Earth pressure is determined according to Jake's equation, i.e., $k_0 = 1 - \sin \varphi$ (φ is the friction angle of soil).

As a major part of the pile shaft was located in strongly weathered granite, direct shear tests were conducted between the concrete structure and the earthy strongly weathered granite; the friction angle was determined to be 27° . However, slurry protected the wall of the pile hole during construction, and a thin layer of slurry cakes formed after the concrete was cast. The slurry cake significantly reduced the interface friction; however, its effect was difficult to quantify as the thickness and properties of slurry cakes were highly uneven around the pile. For this reason, sensitivity analysis was used to determine a suitable interface friction. Three values of α , i.e., 5° , 10° , and 20° , were used to conduct the analysis; Figure 11 presents the results. The value of α significantly affected the axial load distribution along the pile. As the value of α increased, the friction of soil acting on the pile's skin carried more force; correspondingly, the force transferred to the pile end was smaller. For the cast-in-place pile monitored in this study, the friction angle between the soil and the pile was approximately 10° , which is approximately one third of the measured friction angle when the effect of slurry cakes is not considered.

Another issue requiring careful consideration was strain in the shallow section of the pile. The measured strain was found to be unreasonably large, probably due to the complex loading mode. The gradient of the strain against depths between 10 m and 15 m was also too large. As Figure 12 illustrates, fitting all measured data yielded a larger prediction of strain

along the pile and the axial load at the pile head; therefore, measured strain above a depth of 15 m was excluded when interpreting these data, to provide a more reasonable prediction.

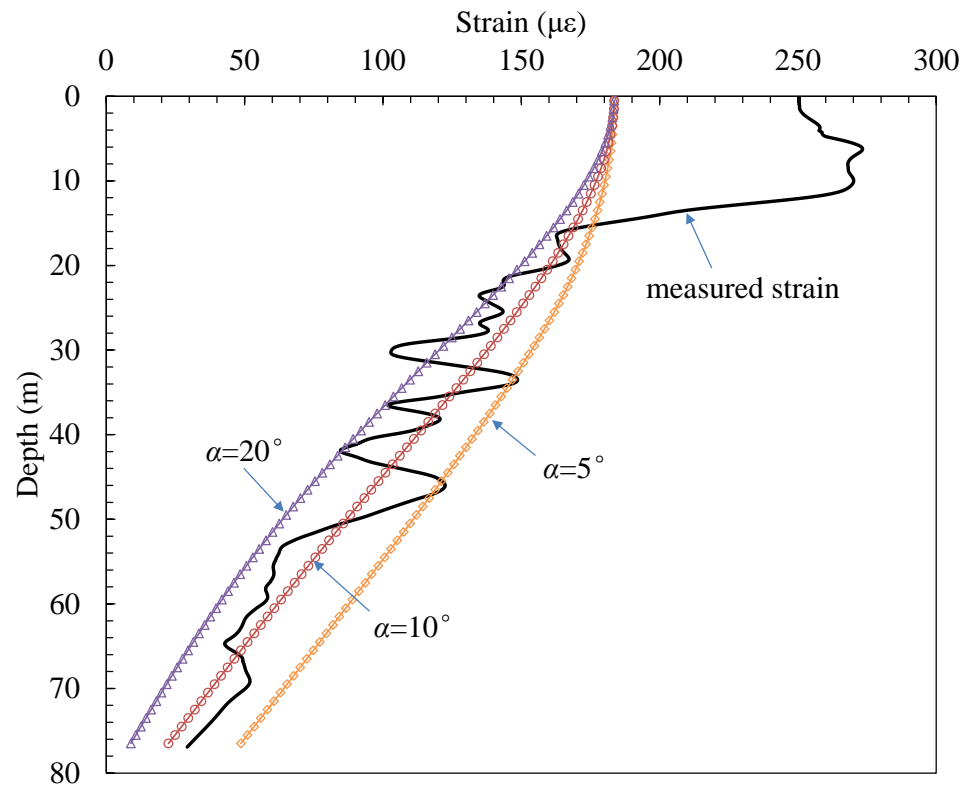


Figure 11. Effect of the friction angle at the interface of soil and pile.

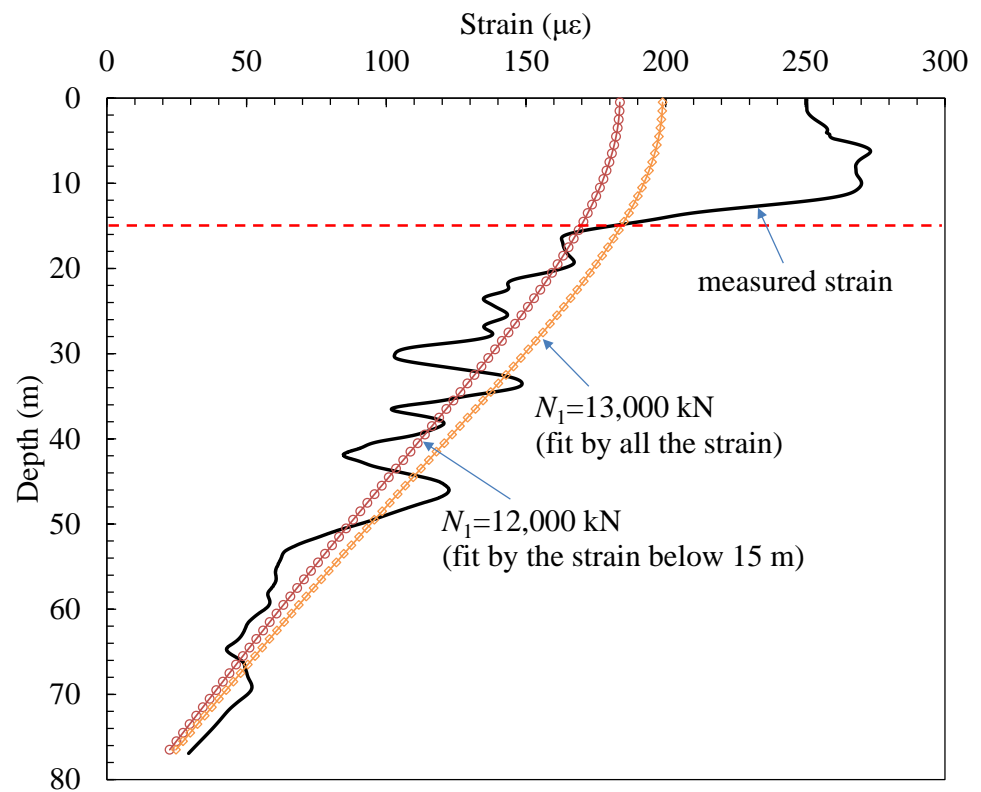


Figure 12. Effect of the data in the shallow section on the fitted axial load.

Data measured on 14 November 2021, 26 November 2021, 5 December 2021, 14 December 2021, 2 January 2022, 19 February 2022, 9 March 2022, 18 May 2022, and 29 May 2022 were processed using the aforementioned method and technique; the fitted strain and calculated axial force along the pile shaft are presented in Figure 13. As expected, processed axial strains were in good agreement with the overall trend in axial strain against the depth, as observed in the measurements. The slope of the axial force with respect to depth at the shallow section seems to be reasonable, which tends to be zero at the ground's surface. The axial force at the end of the pile increased as floors were built and increased the upper load; this indicates that more axial load at the pile head was transferred to the pile end. On 29 May 2022, approximately 12.24% of the axial load exerted on the pile head was carried by the pile end, whereas the other 87.76% of the load was balanced by skin friction. Therefore, the long (76.7 m), large-diameter pile embedded primarily in strongly weathered granite is a typical frictional pile. Figure 14 compares the axial force distribution along the pile with the results from other tests when the axial forces at the pile head are all approximately 12,000 kN. The length of the piles in the tests conducted by Zou and Zhao [22], Wang et al. [23], Li et al. [24], and Feng et al. [25] was 60 m, 80 m, 56.5 m, and 85.7 m, respectively, which fell within the range of super-long piles. The pile investigated by Feng et al. [25] was a steel pipe pile, while the piles in other studies were bored piles. Although the variation in the axial force with the depth shows apparent differences in these studies due to difference in the site conditions and pile geometry, all the results indicate that the skin friction bore the major part of the load exerted at the pile head.

Figure 15 presents axial loads at the pile head and the number of floors built. The estimated axial loads were approximately 1508 kN, 2498 kN, 3185 kN, 3822 kN, 5034 kN, 7516 kN, 8993 kN, 10,522 kN, and 11,897 kN on 14 November 2021, 26 November 2021, 5 December 2021, 14 December 2021, 2 January 2022, 19 February 2022, 9 March 2022, 18 May 2022, and 29 May 2022, respectively. The corresponding numbers of floors built were 13, 17, 19, 20, 24, 28, 31, 36, and 40, respectively. The average axial force exerted on the pile head by one floor during construction was approximately 116.00 kN, 146.94 kN, 167.63 kN, 191.10 kN, 209.75 kN, 268.43 kN, 290.10 kN, 292.28 kN, and 297.43 kN on these dates, respectively. This project used a piled raft foundation. In the early stages of construction, the raft carried a large portion of the load induced by the superstructure. However, as the number of floors built and the total load increased, the piles gradually bore the major portion of the increased load due to continuous construction.

Mobilized skin friction was estimated using the proposed methodology during different stages of construction; Figure 16 presents the results. Mobilized skin friction was initially low along the pile shaft and increased as the vertical load at the pile head increased. Above 10 m, the interface reached the ultimate skin friction on 29 May 2022, but the percentage of mobilization tended to decrease with increasing depth. To evaluate the pile's safety, the overall mobilized percentage (defined as the ratio of integration of mobilized skin friction against the depth to the integration of the ultimate skin friction against the depth) was calculated, and is presented in Figure 17. On 14 November 2021, when there were 13 floors built, the overall mobilized percentage was approximately 5.1%. On 29 May 2022, when there were 40 floors built, the overall mobilized percentage was approximately 40.8%, which indicates that the pile was in a sufficiently safe state in terms of loading capacity.

Finally, to disclose the influence of design parameters on pile behavior under the axial load, sensitivity analyses were conducted with different combinations of pile length, L , and pile diameter, D . The results presented in Figure 18 show the development of skin friction for piles having the same diameter (1.6 m) but different lengths when the axial load at the pile heads is 11897 kN. It is seen that, as the length decreases, the mobilized skin friction at the shallow part approaches the ultimate value quickly. The overall mobilized percentage is approximately 38.0%, 47.1%, 59.2%, 75.1%, and 93.4% for $L = 80$ m, 70 m, 60 m, 50 m, and 40 m, respectively. Figure 19 presents the results for the piles having the same length (76.7 m) but different diameters. It is seen that the mobilized skin friction decreases as the pile diameter increases. The overall mobilized percentage is approximately 53.0%, 46.7%,

40.5%, 35.3%, and 31.1% for $D = 1.2$ m, 1.4 m, 1.6 m, 1.8 m, and 2.0 m, respectively. In view of the results presented in Figures 17 and 18, the pile design can be further optimized in a small range.

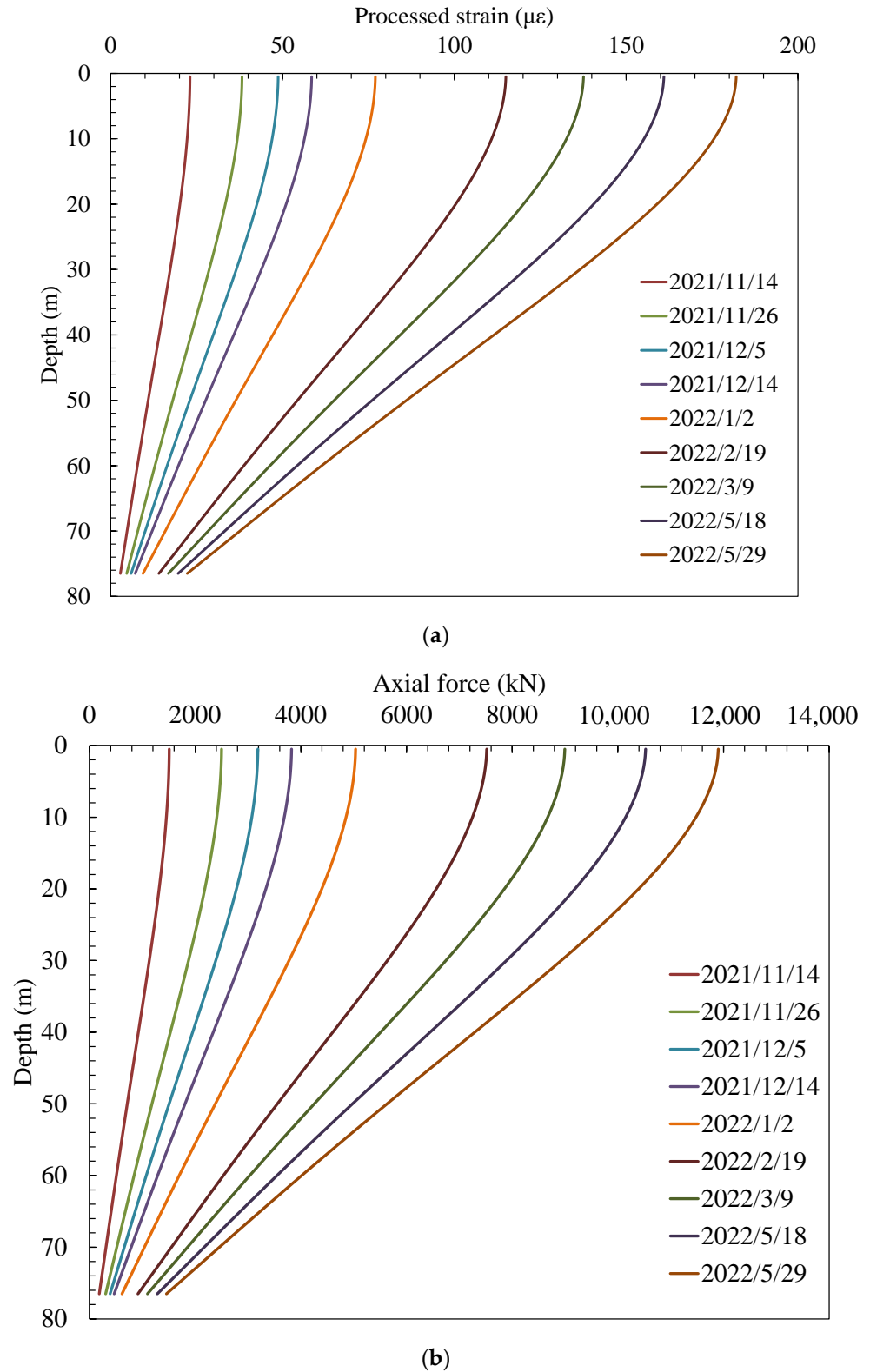


Figure 13. Processed axial strain and axial force along the pile: (a) processed axial strain; (b) axial force.

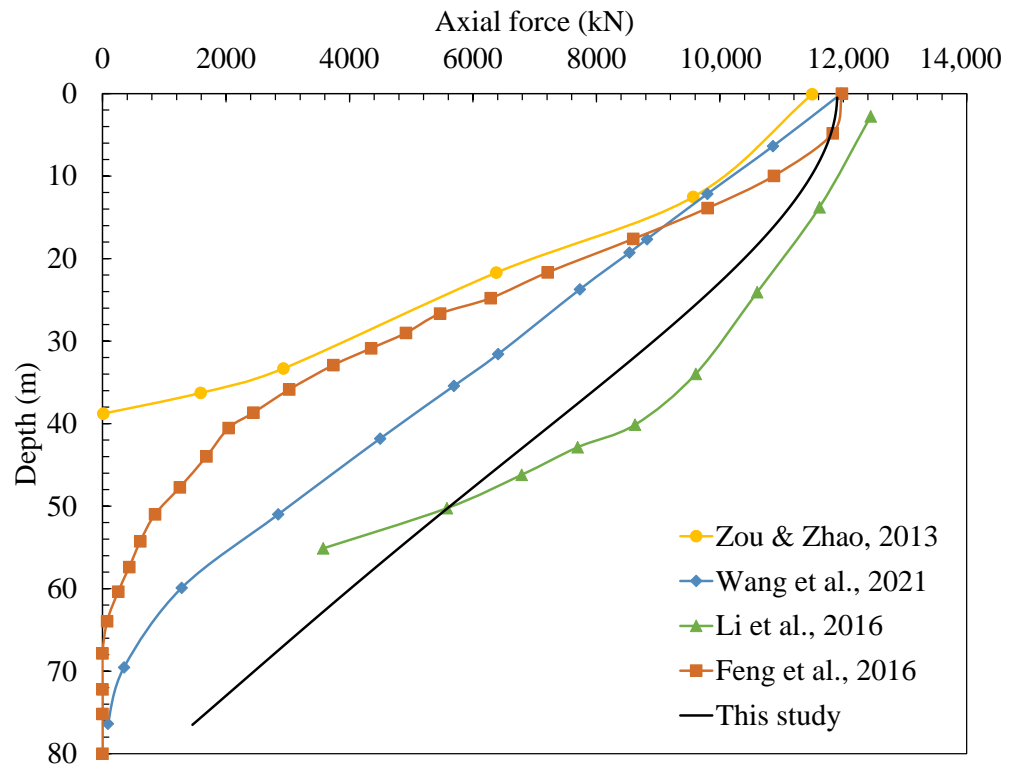


Figure 14. Comparison of the axial force distribution along the pile with the results from other tests [22–25].

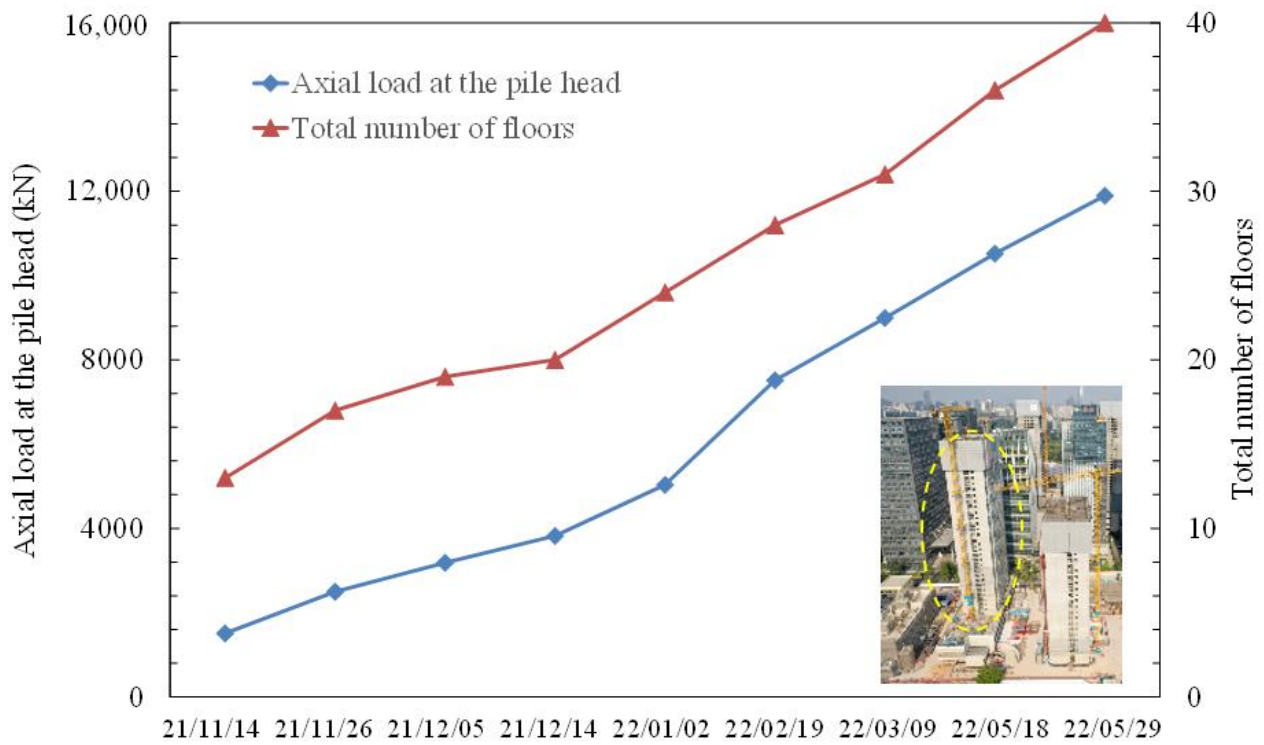


Figure 15. Variation in the axial load at the pile head with the total number of built floors.

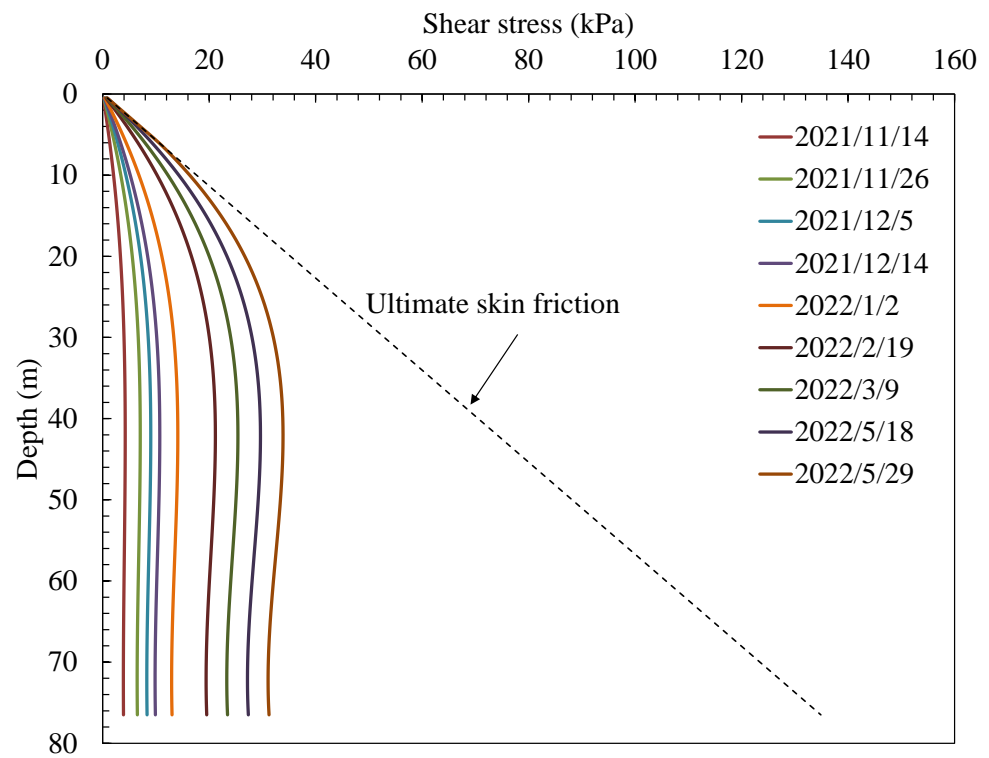


Figure 16. Development of skin friction.

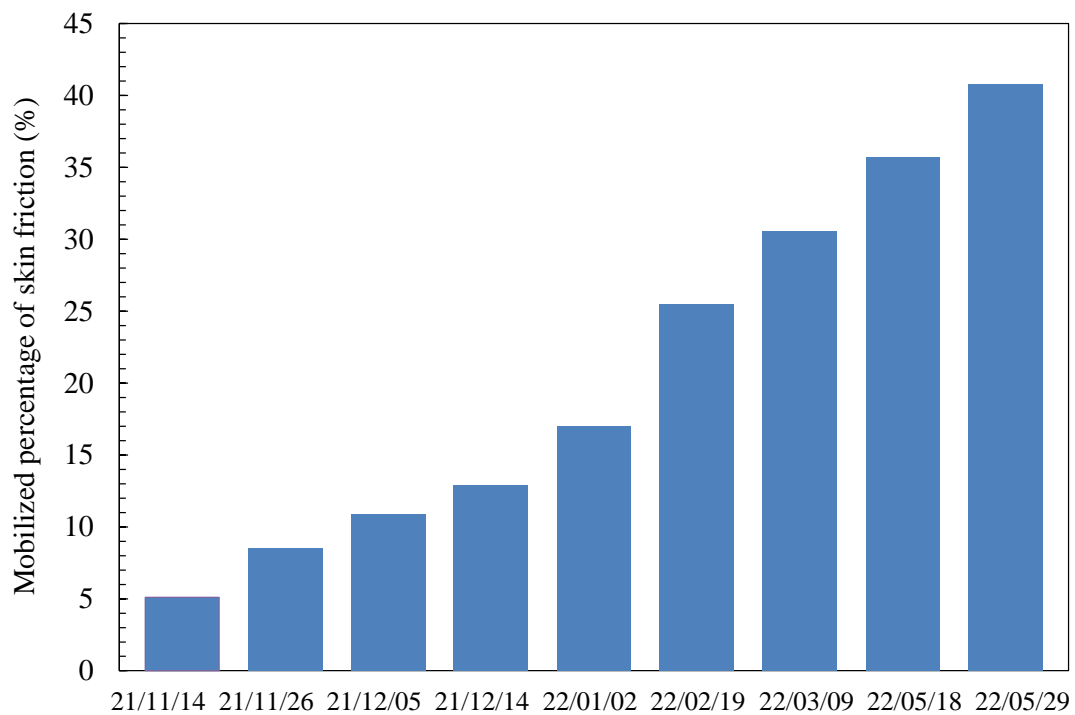


Figure 17. Mobilized percentage of skin friction.

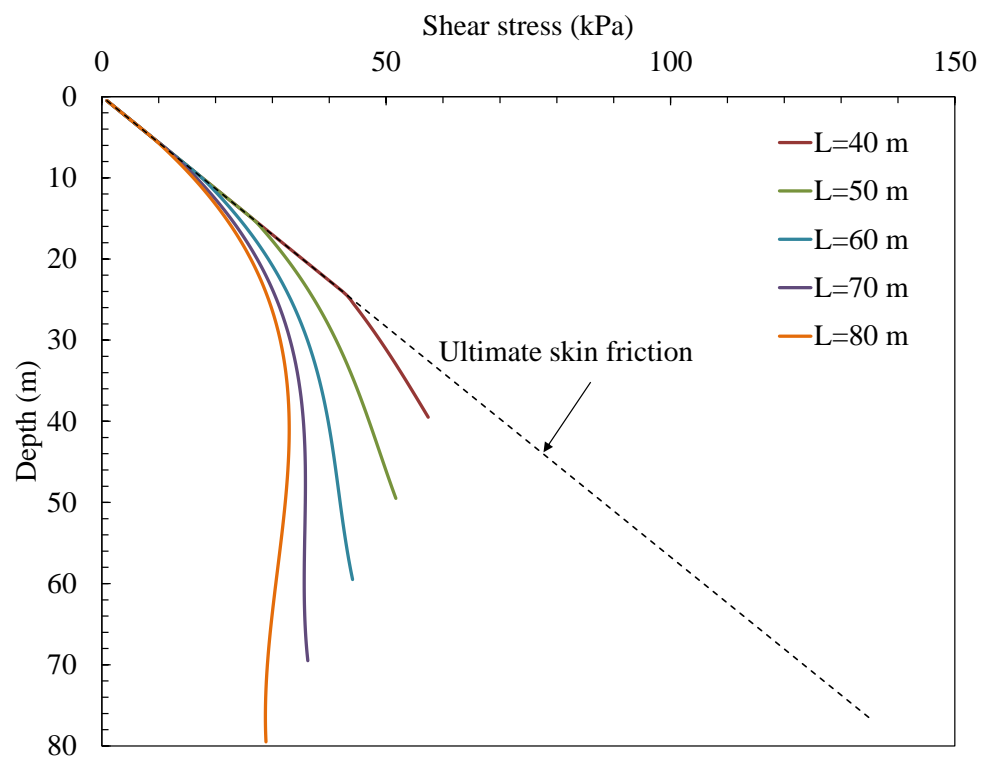


Figure 18. Effect of pile length on development of skin friction.

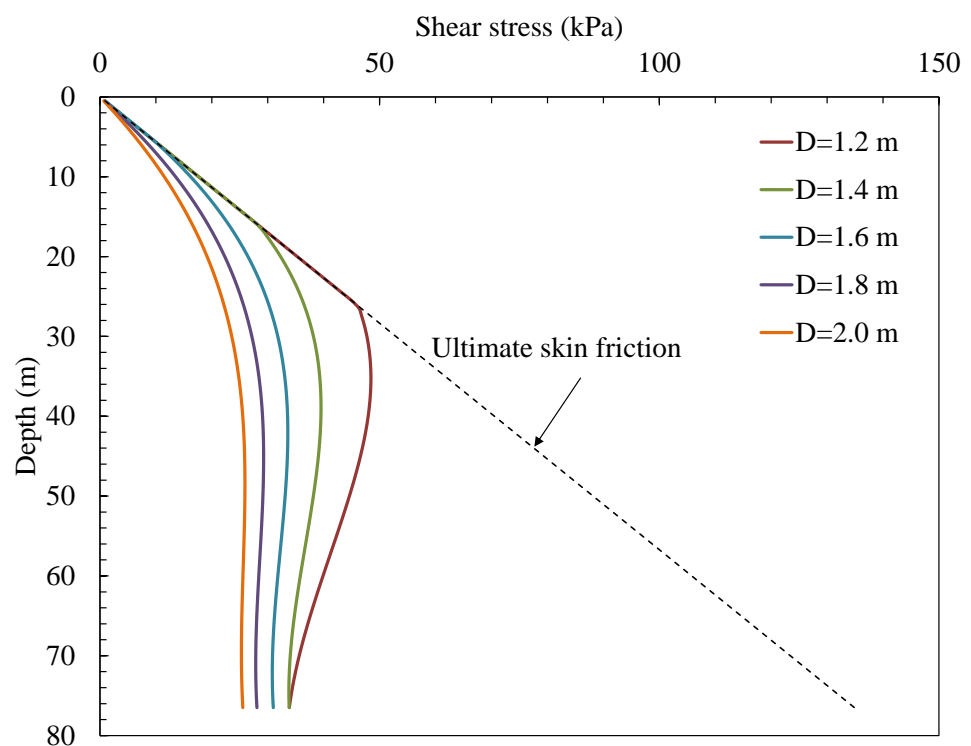


Figure 19. Effect of pile diameter on development of skin friction.

4. Conclusions

The long-term behavior of a super-long cast-in-place pile was measured using BOFDA monitoring technology during the construction of a superstructure. Data were reinterpreted using the proposed method based on the load-transfer mechanism, so that the pile's charac-

teristics and the interface between the pile and the surrounding soil could be determined. The following conclusions can be made based on the study's results:

(1) Measured data can well reflect an increase in axial strain with an increase in the number of floors built. However, unwanted data deviation from the real pile response can be observed in the measured data due to the bending of the fiber cable during concrete installation and compaction. Complex loading conditions at the pile head also make it difficult to interpret data in the pile's shallow section.

(2) Based on the load-transfer method and incorporating the bilinear model for soil–pile interface behavior, the relationship between the force at the top of the pile and the axial strain along the pile can be obtained. Sensitivity analysis of parameters can be conducted using the relationship and measured data to obtain best-fit axial strain distributions. The cast-in-place pile monitored in this study had a friction angle of approximately 10° between the soil and the pile, which is approximately one third of the measured friction angle when the effect of slurry cakes is not considered.

(3) The average axial force exerted on the pile head as induced by one floor during construction ranges from 116.00 kN to 297.43 kN; axial force increases as the number of floors built and the total load increases. When 40 floors were built, the overall mobilized percentage of skin friction was approximately 40.8%, and the pile was in a sufficiently safe state in terms of loading capacity.

Author Contributions: Conceptualization, D.L. and D.M.; Data curation, C.H.; Formal analysis, D.S.; Funding acquisition, D.S.; Investigation, D.L., D.M., S.R., and W.W.; Methodology, D.S. and S.R.; Project administration, D.M.; Validation, W.W.; Writing—original draft, D.S.; Writing—review and editing, D.L. and C.H. All authors have read and agreed to the published version of the manuscript.

Funding: This research work was funded by the Natural Science Foundation of Shenzhen (Grant No. JCYJ20210324094607020).

Institutional Review Board Statement: Not applicable.

Informed Consent Statement: Not applicable.

Data Availability Statement: All data included in this study are available upon request by contact with the corresponding author.

Conflicts of Interest: No potential conflicts of interest were reported by the authors.

References

1. Hoang, L.T.; Matsumoto, T. Long-term behavior of piled raft foundation models supported by jacked-in piles on saturated clay. *Soils Found.* **2020**, *60*, 198–217. [[CrossRef](#)]
2. Mohanty, P.; Dutta, S.; Bhattacharya, S. Proposed mechanism for mid-span failure of pile supported river bridges during seismic liquefaction. *Soil Dynam. Earthq. Eng.* **2017**, *102*, 41–45. [[CrossRef](#)]
3. McVay, M.; Casper, R.; Shang, T. Lateral response of three-row groups in loose to dense sands at 3D and 5D pile spacing. *J. Geotech. Eng.* **1995**, *121*, 436–441. [[CrossRef](#)]
4. McVay, M.; Shang, T.; Casper, R. Centrifuge testing of fixed head laterally loaded battered and plumb pile groups in sand. *Geotech. Test. J.* **1996**, *19*, 41–50.
5. McVay, M.; Zhang, L.; Molnit, T.; Lai, P. Centrifuge testing of large laterally loaded pile groups in sands. *J. Geotech. Geoenviron. Eng.* **1998**, *124*, 1019–1026. [[CrossRef](#)]
6. Patra, N.R.; Pise, P.J. Ultimate lateral resistance of pile groups in sand. *J. Geotech. Geoenviron. Eng.* **2001**, *127*, 481–487. [[CrossRef](#)]
7. Chandrasekaran, S.S.; Boominathan, A.; Dodagoudar, G.R. Group interaction effects on laterally loaded piles in clay. *J. Geotech. Geoenviron. Eng.* **2010**, *136*, 573–582. [[CrossRef](#)]
8. Zhuang, X.; Zong, Z.; Huang, Y.; Wang, P. Analysis of the Installation Effect on the Axial Performance of Pressure-Grouted Helical Piles in Clay by Small-Scale Model Tests. *Buildings* **2022**, *12*, 992. [[CrossRef](#)]
9. McVay, M.; Bloomquist, D.; Vanderlaine, D.; Clausen, J. Centrifuge modeling of laterally loaded pile group in sand. *Geotech. Test. J.* **1994**, *17*, 29–137.
10. Rao, S.N.; Ramakrishna VG, S.T.; Rao, M.B. Influence of rigidity on laterally loaded pile groups in marine clay. *J. Geotech. Geoenviron. Eng.* **1998**, *124*, 542–549. [[CrossRef](#)]
11. Su, D. Resistance of Short, Stiff Piles to Multidirectional Lateral Loadings. *Geotech. Test. J.* **2012**, *35*, 313–329.
12. Cooke, R.W. Piled raft foundations on stiff clays—A contribution to design philosophy. *Geotechnique* **1986**, *36*, 169–203. [[CrossRef](#)]

13. Mandal, S.; Sengupta, S. Experimental investigation of eccentrically loaded piled raft resting on soft cohesive soil. *Indian Geotech. J.* **2017**, *47*, 314–325. [[CrossRef](#)]
14. Rodriguez, E.; Cunha, R.P.; Caicedo, B. Behaviour of piled raft foundation systems in soft soil with consolidation process. *Proc. of the 9th Int. Conf. Phys. Model. Geotech.* **2018**, *2*, 1407–1411.
15. Matlock, H.; Ingmar, W.B.; Kelley, A.E.; Bogard, D. Field Tests of Lateral Load Behavior of Pile Groups in Soft Clay. *Proc. Twelfth Annu. Offshore Technol. Conf. OTC 3871 Houst. Tex.* **1980**, *1204*, 577–594.
16. Brown, D.A.; Reese, L.C. Lateral load behavior of pile group in sand. *J. Geotech. Eng. ASCE* **1988**, *114*, 1261–1276. [[CrossRef](#)]
17. Brown, D.A.; Reese, L.C.; O'Neill, M.W. Cyclic lateral loading of a large-scale pile group. *J. Geotech. Eng. ASCE* **1987**, *103*, 1326–1343. [[CrossRef](#)]
18. Rollins, K.M.; Peterson, K.T.; Weaver, T.J. Lateral load behavior of full-scale pile group in clay. *J. Geotech. Eng. ASCE* **1998**, *124*, 468–478. [[CrossRef](#)]
19. Rollins, K.M.; Olsen, R.J.; Elbert, J.J.; Jensen, D.H.; Olsen, K.G.; Garrett, B.H. Pile spacing effects on lateral pile group behavior: Load tests. *J. Geotech. Geoenviron. Eng.* **2006**, *132*, 1262–1271. [[CrossRef](#)]
20. Sales, M.M.; Small, J.C.; Poulos, H.G. Compensated piled rafts in clayey soils: Behaviour, measurements, and predictions. *Can. Geotech. J.* **2010**, *47*, 327–345. [[CrossRef](#)]
21. Tang, Y.J.; Pei, J.; Zhao, X.H. Design and measurement of piled-raft foundations. *Proc. Inst. Civ. Eng. Geotech. Eng.* **2014**, *167*, 461–475. [[CrossRef](#)]
22. Zou, X.; Zhao, M. Axial bearing behavior of super-long piles in deep soft clay over stiff layers. *J. Cent. South Univ.* **2013**, *20*, 2008–2016. [[CrossRef](#)]
23. Wang, X.; Que, Y.; Wang, K.; Diao, H.; Cui, Y.; Li, Q. A field test scrutiny on bearing mechanism of super-long bored piles in deep fine silty sand layers. *Mar. Georesour. Geotec.* **2021**. [[CrossRef](#)]
24. Li, S.; Zhang, Q.; Zhang, Q.; Li, L. Field and Theoretical study of the response of super-long bored pile subjected to compressive Load. *Mar. Georesour. Geotec.* **2016**, *34*, 71–78. [[CrossRef](#)]
25. Feng, S.; Lu, S.; Shi, Z. Field Investigations of Two Super-long Steel Pipe Piles in Offshore Areas. *Mar. Georesour. Geotec.* **2016**, *34*, 559–570. [[CrossRef](#)]
26. Randolph, M.F. The responses of flexible piles to lateral loading. *Géotechnique* **1981**, *31*, 247–259. [[CrossRef](#)]
27. Zhang, L.; Liu, H. Seismic response of clay-pile-raft-superstructure systems subjected to far-field ground motions. *Soil Dynam. Earthq. Eng.* **2017**, *101*, 209–224. [[CrossRef](#)]
28. Banerjee, S.; Goh, S.; Lee, F. Earthquake-induced bending moment in fixed-head piles in soft clay. *Geotechnique* **2014**, *64*, 431–446. [[CrossRef](#)]
29. Su, D.; Li, J.H. Three-dimensional finite element study of a single pile response to multidirectional lateral loadings incorporating the simplified state-dependent dilatancy model. *Comput. Geotech.* **2013**, *50*, 129–142. [[CrossRef](#)]
30. Matlock, H. Correlations for design of laterally loaded piles in soft clay. In Proceedings of the 2nd Offshore Technology Conference, Houston, TX, USA, 22–24 April 1970; pp. 577–594.
31. Su, D.; Yan, W.M. Relationship between p-multiplier and force ratio at pile head considering nonlinear soil-pile interaction. *Géotechnique* **2019**, *69*, 1019–1025. [[CrossRef](#)]
32. Roy, J.; Kumar, A.; Choudhury, D. Natural frequencies of piled raft foundation including superstructure effect. *Soil Dynam. Earthq. Eng.* **2018**, *112*, 69–75. [[CrossRef](#)]
33. Zhou, W.; Wang, L.; Guo, Z.; Liu, J.; Rui, S. A novel t-z model to predict the pile responses under axial cyclic loadings. *Comput. Geotech.* **2019**, *112*, 120–134. [[CrossRef](#)]
34. Zhou, W.; Guo, Z.; Wang, L.; Li, J.; Rui, S. Simplified t-z models for estimating the frequency and inclination of jacket supported offshore wind turbines. *Comput. Geotech.* **2021**, *132*, 103959. [[CrossRef](#)]
35. Bao, X.; Chen, L. Recent progress in distributed fiber optic sensors. *Sensors* **2012**, *12*, 8601–8639. [[CrossRef](#)]
36. Gao, L.; Shi, B.; Zhu, Y.; Wang, K.; Sun, Y.; Tang, C. A distributed soil temperature measurement system with high spatial resolution based on BOTDR. *Opt. Appl.* **2011**, *3*, 607–616.
37. Pei, H.F.; Yin, J.H.; Zhu, H.H.; Hong, C.Y.; Jin, W.; Xu, D.S. Monitoring of lateral displacements of a slope using a series of special fiber Bragg grating-based in-place inclinometers. *Meas. Sci. Technol.* **2012**, *23*, 025007. [[CrossRef](#)]
38. Zhu, H.H.; Shi, B.; Yan, J.F.; Zhang, J.; Wang, J. Investigation of the evolutionary process of a reinforced model slope using a fiber-optic monitoring network. *Eng. Geol.* **2015**, *186*, 34–43. [[CrossRef](#)]
39. Lei, G.; Kai, Y.; Chen, X.; Yu, X. Study on the deformation measurement of the cast-in-place large-diameter pile using fiber bragg grating sensors. *Sensors* **2017**, *17*, 505.
40. Liu, Y.; Li, H.; Wang, Y.L.; Men, W.Q.; Xu, Q.E. Damage detection of tunnel based on the high-density cross-sectional curvature obtained using strain data from BOTDA sensors. *Mech. Syst. Signal. Process.* **2021**, *158*, 1077281–10.
41. Gao, L.; Cao, Y.; Liu, H.L.; Zhao, Z.X.; Ye, Y.F.; Fan, C.J.; Tu, W.J. Experiment and numerical study on the monitoring of super long cast-in-place pile temperature based on BOTDR technology. *Measurement* **2021**, *179*, 109481. [[CrossRef](#)]
42. Zhang, Q.H.; Xiong, Z.M. Crack detection of reinforced concrete structures based on BOFDA and FBG sensors. *Shock. Vib.* **2018**, *2018*, 6563537. [[CrossRef](#)]
43. Cheng, L.; Zhang, A.A.; Cao, B.L.; Yang, J.; Hu, L.C.; Li, Y.L. An experimental study on monitoring the phreatic line of an embankment dam based on temperature detection by OFDR. *Opt. Fiber. Technol.* **2021**, *63*, 102510. [[CrossRef](#)]

44. Zhang, D.; Cui, H.; Shi, B. Spatial resolution of DOFS and its calibration methods. *Opt. Lasers Eng.* **2013**, *51*, 335–340. [[CrossRef](#)]
45. Gao, L.; Gong, Y.H.; Liu, H.L.; Ji, B.Q.; Xuan, Y.N.; Ma, Y. Experiment and Numerical Study on Deformation Measurement of Cast-in-Place Concrete Large-Diameter Pipe Pile Using Optical Frequency Domain Reflectometer Technology. *Appl. Sci.* **2018**, *8*, 1450. [[CrossRef](#)]
46. Liu, Q.S.; Wang, J.T.; Xiao, L.G.; Li, J.C.; Liu, B.; Zhang, X.L. The application of OFDR optical fiber sensing technology in the physical model test of cross rock pillar excavation method. *J. Rock Mech. Eng.* **2017**, *36*, 1063–1075. [[CrossRef](#)]
47. Wei, C.; Deng, Q.; Yin, Y.; Yan, M.; Lu, M.; Deng, K. A Machine Learning Study on Internal Force Characteristics of the Anti-Slide Pile Based on the DOFS-BOTDA Monitoring Technology. *Sensors* **2022**, *22*, 2085. [[CrossRef](#)]